JACS
JOURNAL OF THE AMERICAN CHEMICAL SOCIETY
pubs.acs.org/JACS
Article

Ion-Modulated Ostwald Ripening Dynamics of Nitrogen Nanobubble Pairs

Xiangdang Guo, Pengchao Zhang,* Chao Sun,* and Xuefei Xu*

Cite This: J. Am. Chem. Soc. 2026, 148, 32412−32425
Read Online
ACCESS | Metrics & More | Article Recommendations | Supporting Information

ABSTRACT: Understanding the stability of bulk nanobubbles, especially how electrolyte ions influence their coarsening dynamics, holds significant importance for widespread practical applications, but the fundamental microscopic mechanisms remain not fully understood and warrant further investigation. In this work, using machine-learning molecular dynamics simulations, we captured the Ostwald ripening of bulk nanobubbles, which is consistent with experimental observations, and systematically investigated its behavior under neutral, acidic, alkaline, and saline conditions. Notably, the ripening rates exhibit a system-dependent order: acidic > alkaline ≈ pure water > saline. Further analyses reveal that counterions critically regulate the orientational alignment and hydrogen bonding of interfacial water molecules and ions through hydration and electrostatic effects. Furthermore, in the saline system, the coupling of Na^+ and Cl^- ions leads to the enrichment of "lying-flat" ion pairs near the interface, forming a dense hydration layer. Based on how these interfacial structural alterations regulate gas diffusion to impact the bubble ripening rate, we established an ion-modulated microscopic mechanism grounded in the relative dominance of enthalpy and entropy. This framework, which incorporates specific-ion effects, provides a self-consistent explanation for the divergent ripening rates observed across various environments. Ultimately, these findings bridge atomistic interfacial restructuring with thermodynamic principles, providing a comprehensive physicochemical landscape for understanding ion-modulated nanobubble coarsening dynamics.

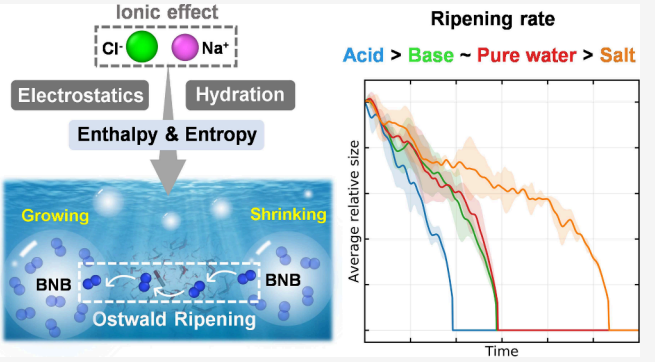

1. INTRODUCTION

Bulk nanobubbles (BNBs) are nanoscopic gas domains dispersed in liquids. Due to their exceptional longevity, high specific surface area, and significant surface zeta potential, BNBs have attracted sustained interest in various fields, such as separation,[1−3] catalysis,[4,5] cleaning,[6,7] and biomedical processes.[8−10] At the same time, their reported stability confronts a central paradox in bubble physics. According to the classical Epstein−Plesset theory, the high curvature of BNBs implies the Laplace pressure on the order of tens of MPa, which should drive rapid dissolution in microseconds to milliseconds. However, experiments have consistently shown that BNBs can remain stable for hours or even days. This stability paradox has motivated several theoretical explanations, including the dense skin model,[11,12] the diffusion shielding mechanism,[13] and the surface charge model.[14,15] Key parameters in these models, such as the effective interfacial permeability, local gas supersaturation fields, and the interfacial ion adsorption state, are difficult to measure independently. Moreover, the applicability of these explanations is often restricted to specific regimes and assumptions. These limitations not only leave the universal microscopic stabilization mechanism of BNBs unresolved, but also imply that the single-bubble framework may be insufficient.

BNBs typically exist as dispersions characterized by a finite number density rather than as isolated objects. Their apparent stability is therefore inseparable from the temporal evolution of the size distribution, which reflects both single-bubble dissolution dynamics and interbubble interactions. Existing studies reported markedly divergent evolution scenarios depending on gas type, electrolyte composition, surfactant coverage, and generation protocols.[16−22] A mean-field theory for computing the evolution of size distribution of BNBs suggested that sufficient surfactant adsorption can lead to a gradual decrease in the average bubble size;[16] Alternatively, ultrasonic cavitation in nominally pure water has been reported to yield an approximately time-invariant size distribution of BNBs, while the peak intensity decays.[17] However, more commonly, experiments observed coarsening of BNBs, that is, the average bubble size increases while the number density

Received: April 29, 2026
Revised: June 24, 2026
Accepted: July 13, 2026
Published: July 22, 2026

decreases over time,[18−20] sometimes accompanied by an approximately conserved total gas volume[21] or the emergence of discrete peaks in the size distribution.[22] The macroscopic coarsening of the dispersed phase is a process fundamentally driven by the minimization of total interfacial energy. From a microscopic perspective, this coarsening implies a propensity of bubbles to merge upon approach, a phenomenon explicitly corroborated by theoretical and simulation studies.[23−26] However, multiple microscopic pathways may cause BNBs coarsening, for example, interbubble mass transfer and collision-mediated bubble encounters, and the interfacial physicochemistry can tilt the balance among these pathways.

For colloidal dispersions, two predominant dynamics ways of coarsening are commonly discussed. One is Ostwald ripening, which describes the growth of larger objects at the expense of smaller ones through molecular diffusion in the continuous phase.[27] The other is Smoluchowski ripening that describes aggregation via Brownian-motion-induced collisions.[28] In the context of bubbles, the latter is more naturally interpreted as coalescence (hereafter synonymous with Smoluchowski ripening), and ripening will be used exclusively as shorthand for the Ostwald ripening in this work.

The two aforementioned coarsening mechanisms have been widely applied to investigate issues such as the diffusion and sintering of nanoparticles on solid surfaces,[29,30] as well as the fabrication and preservation of nanoparticles.[31,32] Analogous arguments have also been applied to microbubble populations[33,34] and surface nanobubbles.[35,36] However, BNBs differ from microbubbles and surface nanobubbles in several key aspects. Unconstrained by substrates and free-floating in the bulk, BNBs are characterized by ultrahigh curvature and elevated interfacial gas density. Furthermore, these unique interfacial characteristics make BNBs highly sensitive to environmental factors such as surfactants, pH, and ionic species and strength. In particular, ions are ubiquitous in realistic aqueous systems and have been shown to influence BNB-related phenomena, driven by their specific hydration properties[37] and interfacial adsorption behaviors.[14,15,38,39] Crucially, such ionic modulation of nanobubble behavior might be pivotal in diverse scenarios, such as electrochemical systems, where bulk nanobubbles near electrodes may influence reaction efficiency,[40] and marine environments, where these suspended bubbles mediate organic pollutant removal.[41] Given this critical context, a central question remains insufficiently addressed: how do specific ions regulate interbubble interactions and coarsening dynamics by restructuring the gas−liquid interface?

Unfortunately, progress on answering this question has been hindered by both experimental and theoretical constraints. Experimentally, measurements predominantly focus on macroscopic statistics such as number density and size distributions, which capture collective behavior but obscure specific microscopic mechanisms. Moreover, elementary events of coarsening are difficult to resolve with sufficient spatiotemporal detail.[42−44] Theoretically, molecular dynamics (MD) simulations can resolve atomistic mechanisms, but many existing studies employ classical force fields,[45−47] which may not capture electrolyte-specific interfacial restructuring with the fidelity needed to connect ion effects to quantitative mass-transfer dynamics. Therefore, an atomistically resolved yet accurate description of gas−electrolyte interfaces is essential for building a mechanistic, testable link between specific-ion effects and BNBs coarsening. Recent advances in machine-learning interatomic potentials offer a promising way to bridge this gap by approaching *ab initio* accuracy at near-classical MD cost,[48−50] extending the spatiotemporal scales accessible to atomistic simulations. Consequently, such potentials have been widely adopted in modeling aqueous physicochemical processes.[51−53]

In this work, we trained an ion-aware machine-learning potential to investigate how ionic environments regulate N_2 nanobubbles interaction. We employed the DP-GEN framework[54] to generate training data with high-precision energy and force labels, and then fine-tuned the NEP89 foundation model[55,56] to construct a neuroevolution potential (NEP) model that explicitly incorporates counterions. Using this model, we conducted graphics-processing-unit molecular dynamics (GPUMD)[57] simulations for both single-bubble and two-bubble systems in neutral water, acidic (HCl), alkaline (NaOH) and saline (NaCl) solutions. We identified an Ostwald ripening process in dynamic evolution of nanobubble pairs that is consistent with experimentally reported ripening behaviors.[58] We further quantified the ripening dynamics and analyzed the interfacial microstructures in different environments to identify the thermodynamic origins of ion-regulated gas diffusion. Our results reveal that specific counterions govern gas transport via distinct mechanisms: in acidic and alkaline conditions, they drive a coupled restructuring of interfacial water and OH^-/H_3O^+ orientations, whereas in saline solutions, interfacial Na^+-Cl^- coupling creates a barrier that suppresses radial gas diffusion through the ionic hydration shells and markedly retards Ostwald ripening. Together, these findings provide an atomic-scale physicochemical picture connecting specific-ion effects to BNBs coarsening and stability, and establish the fine-tuned NEP model as a reliable tool for simulating complex gas−electrolyte interfaces.

2. COMPUTATIONAL DETAILS

2.1. Data Set Building

In this work, the data set was constructed and expanded using a concurrent learning approach with DP-GEN, which primarily involves three stages: Deep Potential (DP) training with DeePMD-kit,[48] conformational exploration via DPMD in LAMMPS,[59] and labeling of sampled conformation using density functional theory (DFT) calculations in VASP.[60]

The strongly constrained and appropriately normed (SCAN) semilocal density functional has demonstrated significant advantages in describing not only the electronic properties and dynamical behavior of water[61−63] but also ion−water interactions.[64−66] Therefore, we adopted the SCAN functional for the DFT labeling. In the DFT calculations, the plane-wave basis set cutoff was set to 600 eV, the Brillouin zone was sampled at the Γ point only, and the convergence criterion for the electronic self-consistent cycle was set to 1.0×10^{-5} eV. During the DPMD conformational exploration stage, to ensure adequate sampling of diverse configurations, we performed simulations in a canonical ensemble at multiple temperature points. We ultimately obtained a data set comprising 327,177 configurations across 36 subsystems (Table S1), covering gas-phase, bulk-solution, and gas−liquid interface environments. Then we applied the farthest point sampling (FPS)[67] method to reduce the dimensionality of the data set and extracted 6,706 representative configurations, yielding a refined training set.

https://doi.org/10.1021/jacs.6c08865
J. Am. Chem. Soc. 2026, 148, 32412−32425

Similarly, we constructed a representative test set by extracting from the rest of the complete data set using the FPS method.

2.2. NEP89 Model Fine-Tuning

Rather than undertaking the delicate yet time-consuming task of constructing a data set from scratch which balances size and configurational variety well, we opted to fine-tune the NEP89 foundation model[56] based on the aforementioned refined training data set. This strategy efficiently leverages the robustness and universality of the pretrained model while adapting it to our specific system. Accuracy tests conducted on the test set show that the fine-tuned NEP model (hereafter, we will call it NEP-B for convenience) achieves an RMSE of 94 meV/Å for force and an RMSE of 3 meV/atom for atomic energy of the system (Figure S1). Although the NEP-B model exhibits a modest reduction in accuracy compared to the trained DP model, which yields corresponding RMSEs of 40 meV/Å and 1.17 meV/atom, its performance remains within the same order of magnitude. Importantly, the NEP-B model provides a substantial computational speedup of approximately 7-fold for the later molecular dynamics simulations compared to the DP model (Table S2). These results indicate that the NEP-B model effectively balances accuracy and computational efficiency while maintaining the model's generalization capability, which constitutes our primary motivation for switching from DP model to the NEP model for the subsequent large-scale MD production runs.

We further validated the NEP-B model through additional analysis. As shown in Figure S3, the O−O, N−O, Na−O, and Cl−O radial distribution functions (RDFs) calculated from the NaCl system (0.22 M) using the NEP-B model agree well with those from previous simulations.[68−70] We also calculated the diffusion coefficient of N_2 in water, which is nearly identical to our previous DPMD simulation result[65] and remains on the same order of magnitude as the experimental value.[71] These results support the reliability of the NEP-B model in describing both local molecular structures and N_2 transport dynamics. More details are provided in the Supporting Information (SI).

2.3. GPUMD Simulation

Based on the NEP-B model, we performed molecular dynamics simulations using the GPUMD package[57] to investigate bubble stability and interaction mechanisms. First, to evaluate the stability of single nanobubble, we directly used the well-relaxed initial configurations in pure water, acidic, and alkaline environments from our previous work.[65] These systems consist of a cubic simulation cell with a side length of L = 5.5 nm, containing a central N_2 nanobubble (radius $R \approx$ 1.5 nm, comprising 120 N_2 molecules). The counterions (Na^+ and Cl^-) were introduced by uniformly replacing selected water molecules in the bulk phase of these initial configurations. Subsequently, these single-nanobubble systems underwent a further relaxation and equilibration process to ensure a thermodynamically stable state. Then, to explore the microscopic interactions between bubbles, the double-bubble systems were constructed by directly replicating the fully equilibrated single-nanobubble cells along the x-axis, as illustrated in Figure 1. The specific particle compositions for all the simulated single- and double-bubble electrolyte systems are detailed in Table 1.

All simulations were conducted in the isothermal−isobaric (NPT) ensemble, with the pressure maintained at 1 atm and the temperature at 330 K. This temperature is 30 K higher than the target value of 300 K to compensate for the known deviation of the SCAN functional in describing liquid water.[72−74] The elevated temperature may affect the absolute stability and dynamical time scale of nanobubbles; however, because the same temperature was used for all systems, the relative comparison among different aqueous environments is expected to remain meaningful. The pressure and temperature

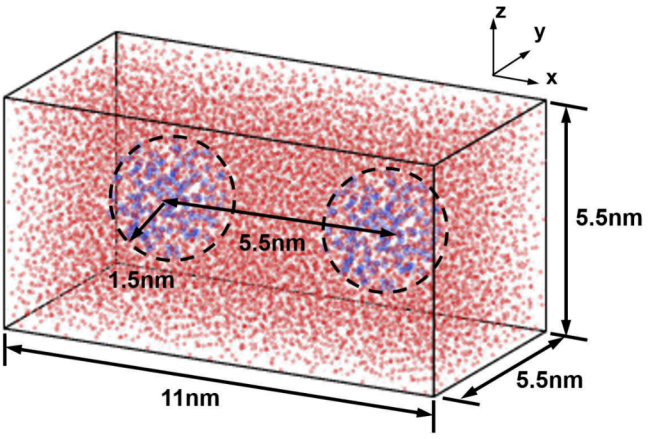

Figure 1. Schematic representation of the double-bubble simulation system. The simulation cell, with dimensions of 11 × 5.5 × 5.5 nm^3, contains two nitrogen nanobubbles characterized by an initial radius of 1.5 nm and a center-to-center separation of 5.5 nm. Color coding: H, white; O, red; N, blue. The surrounding water molecules are rendered semitransparent to clearly visualize the nitrogen configuration within the bubbles.

Table 1. Details of the Simulation Systems

System[a]	Solution Composition[b]	N_2 Count	Num. of Traj.[c]
Pure water (2BNs)	10188 H_2O (0)	240	3(7)
HCl (2BNs)	10108 H_2O + 40 H_3O^+ + 40 Cl^- (0.22 M)	240	3(4)
NaOH (2BNs)	10108 H_2O + 40 Na^+ + 40 OH^- (0.22 M)	240	3(6)
NaCl (2BNs)	10108 H_2O + 40 Na^+ + 40 Cl^- (0.22 M)	240	3(5)
NaCl-2 (2BNs)	10168 H_2O + 10 Na^+ + 10 Cl^- (0.056 M)	240	1(1)
H_3O^+ (2BNs)	10148 H_2O + 40 H_3O^+ (0.22 M)	240	1(1)
OH^- (2BNs)	10148 H_2O + 40 OH^- (0.22 M)	240	1(1)
Pure water (BNs)	5094 H_2O (0)	120	3
HCl (BNs)	5054 H_2O + 20 H_3O^+ + 20 Cl^- (0.22 M)	120	3
NaOH (BNs)	5054 H_2O + 20 Na^+ + 20 OH^- (0.22 M)	120	3
NaOH-2 (BNs)	4854 H_2O + 100 Na^+ + 100 OH^- (1.11 M)	120	3
NaCl (BNs)	5054 H_2O + 20 Na^+ + 20 Cl^- (0.22 M)	120	3

[a]"2BNs" denotes a system containing two equal-sized bulk nanobubbles; "BNs" represents a system with a single bulk nanobubble. [b]The exact counts of solvent molecules and solute ions included in systems. The value in parentheses indicates the molar concentration of the electrolyte solution, with 0 denoting pure water. [c]The number of independent production runs performed for each case. For the double-bubble systems, the value is given as $x(y)$, where x is the number of trajectories exhibiting Ostwald ripening and y is the total number of simulated trajectories.

https://doi.org/10.1021/jacs.6c08865
J. Am. Chem. Soc. 2026, 148, 32412−32425

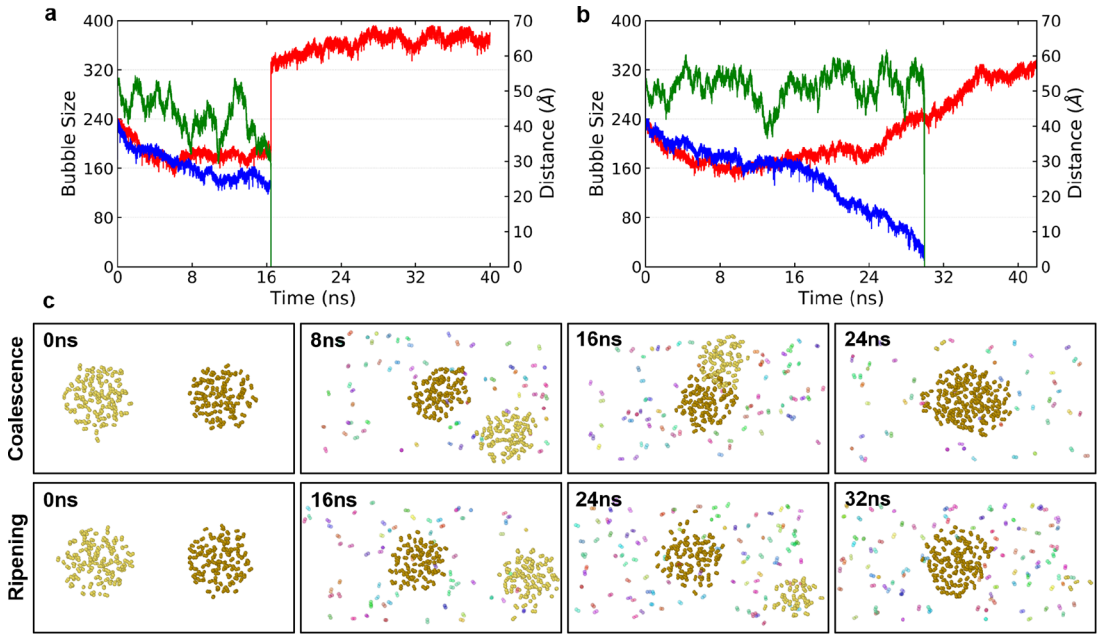

Figure 2. Characterization of the two distinct interaction modes between initially equal-sized bubbles. (a) Time evolution of bubble sizes (number of N atoms) and interbubble distance during the coalescence process. The red and blue curves represent the larger (growing) and smaller (shrinking) bubbles, respectively, while the green curve tracks the distance between their centers of mass. (b) Time evolution of bubble sizes and distance during the Ostwald ripening process, following the same color scheme as in (a). (c) Simulation snapshots visualizing the nitrogen distribution. Molecules belonging to the large and small bubbles are colored dark brown and light yellow, respectively, while dissolved nitrogen molecules in the bulk phase are shown in other colors. Panels (a) and (b) are based on one representative coalescence trajectory and one representative ripening trajectory in the alkaline system, respectively, while panel (c) shows snapshots from these two representative trajectories.

were controlled using the stochastic cell rescaling barostat[75] and the velocity rescaling thermostat,[76] with damping time constants of 1 and 0.1 ps, respectively. A canonical ensemble (*NVT*) simulation was performed for comparison, showing that the ensemble effect is minor for the present analysis, as detailed in the SI.

Due to the varying time scales of bubble dissolution and interaction events across different systems, the total simulation time ranged from 32 to 88 ns. The time step was set to 1 fs, with a general trajectory sampling interval of 1 ps. However, since hydrogen bond (HB) dynamics typically occurs on the picosecond time scale, a finer sampling interval of 0.1 ps was specifically employed for subsequent HB analyses to accurately capture their fast kinetics.

For each single-bubble system, three independent trajectories were simulated. For each investigated double-bubble system, four to seven independent production runs were performed to obtain three trajectories exhibiting the Ostwald ripening process. Unless otherwise specified, all subsequent structural and dynamical analyses of the double-bubble systems were averaged over these three ripening trajectories for each aqueous environment. For each selected trajectory, only the ripening period from the onset of continuous dissolution of the smaller bubble to its complete disappearance was used, and both the shrinking and growing bubbles were included in the statistical averaging. To examine the influence of salt concentration, an additional low-concentration NaCl double-bubble system was simulated, with the NaCl concentration reduced to one-quarter of that normally used in the 0.22 M NaCl double-bubble system. Additionally, to elucidate the specific effects of counterions, one extra trajectory was simulated for each of the acidic and alkaline systems, in which only hydronium or hydroxide ions were included without their corresponding counterions (Cl^- or Na^+).

Further computational details refer to Table 1 and the SI.

3. RESULTS AND DISCUSSION

3.1. Ripening and Coalescence Processes of Double Nanobubbles

In double-bubble simulations, two distinct interaction modes between two bubbles are observed for all investigated systems. We take the alkaline system as an example and show its representative trajectories and selected snapshots in Figure 2. The first mode is bubble coalescence (Figure 2a), characterized by the gradual approach of two nanobubbles followed by their instantaneous merger into a single larger entity. The second mode follows Ostwald ripening (Figure 2b): nitrogen molecules diffuse from the shrinking bubble into the bulk phase and are subsequently adsorbed by the growing bubble, eventually leading to the complete dissolution of the smaller bubble. This dynamic evolution qualitatively agrees with the in situ transmission electron microscopy observations of nanobubble growth dynamics.[58] Note that throughout this study, the size of a nanobubble is quantitatively characterized by the number of constituent nitrogen atoms, and the assignment of nitrogen molecules to each bubble is determined via cluster analysis. The two modes of interaction are visualized in the molecular snapshots in Figure 2c.

The precise onset of coalescence can be evidently identified by a sharp discontinuity in the bubble size evolution once a critical proximity is reached. Given that these coalescence events occur stochastically and can be understood in terms of the well-known Brownian-collision mechanism,[28] in this work, we focus on the complementary coarsening pathway, namely Ostwald ripening, which has been much less explored for

https://doi.org/10.1021/jacs.6c08865
J. Am. Chem. Soc. 2026, 148, 32412−32425

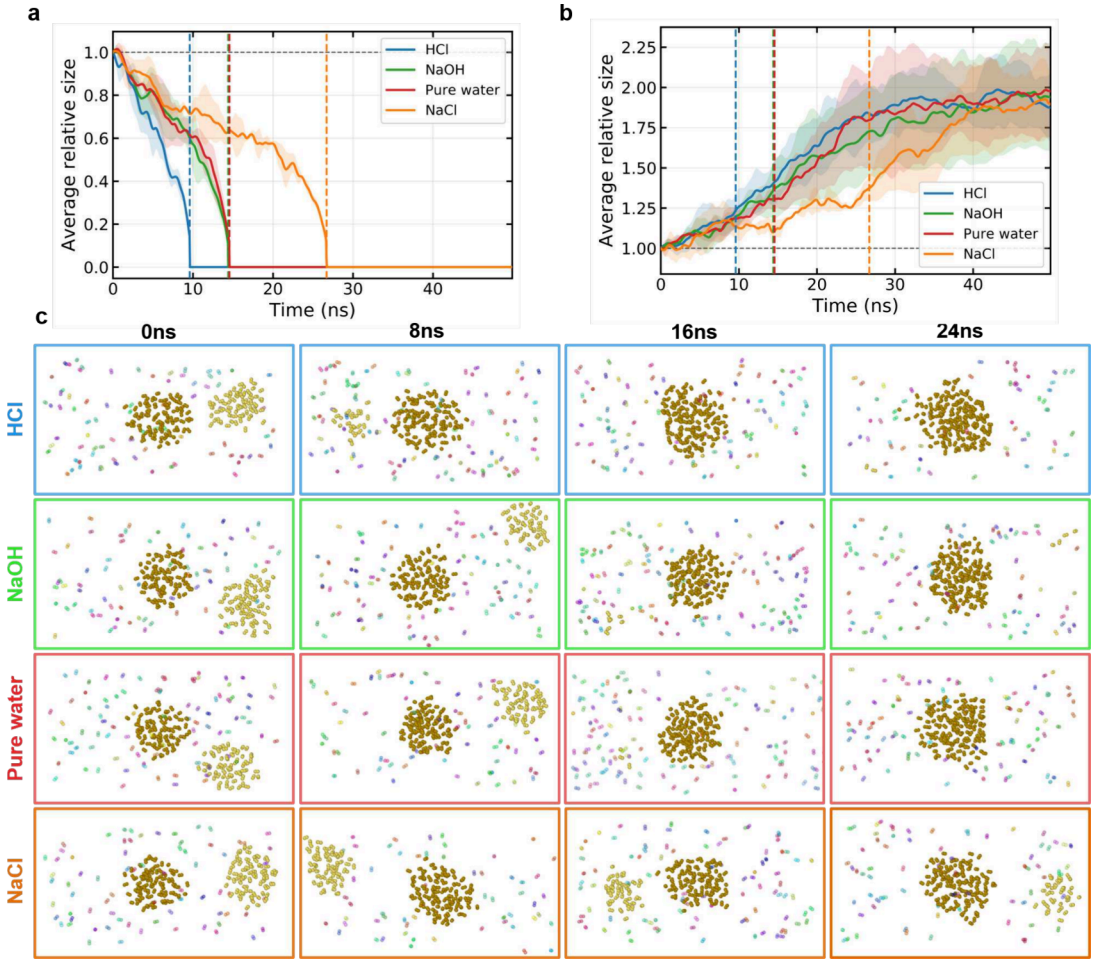

Figure 3. Comparison of ripening dynamics across acidic, alkaline, saline, and pure water systems. (a,b) Temporal evolution of the bubble sizes relative to those at the onset of ripening in the (a) shrinking (small) and (b) growing (large) bubbles. The vertical dashed lines mark the critical moment of complete extinction of the smaller bubble. (c) Simulation snapshots illustrating the bubble evolution at various time points for each system, where dark brown and light yellow N_2 molecules constitute the large and small bubbles, respectively, while N_2 molecules in other colors represent dissolved nitrogen molecules in the bulk phase. Panels (a) and (b) show the averages over three independent ripening trajectories for each system with standard deviations, while panel (c) shows one representative ripening trajectory for each system.

nanobubble pairs, in particular from a microscopic aspect. As shown in Figure 2b, although the two BNBs are initially constructed with equal sizes, microscopic thermal fluctuations gradually give rise to a size asymmetry during the ripening process. Meanwhile, the two bubbles consistently maintain a measurable separation distance (green line), indicating that mass transfer between the two bubbles is mediated by the continuous medium rather than direct contact. We quantitatively substantiated this via a molecular-level Markov transition analysis.[77] Specifically, N_2 molecules in the systems were classified into three states: bubble-1, bubble-2, and bulk states. The analysis reveals that the probability of a direct state transition of N_2 molecules from one bubble state to the other without passing through the bulk state is negligible (Figure S5), confirming that molecular exchange between the two bubbles during the ripening process is predominantly achieved via diffusion through the bulk phase. In addition, the Tolman-corrected total surface energy of the BNBs decreases as ripening proceeds (Figure S6), providing thermodynamic support for Ostwald ripening as a pathway of BNBs coarsening. Relevant details are provided in the SI.

Although all observed ripening processes for a given system exhibit similar characteristics, their onset times vary substantially among independent trajectories (Figure S7a). Here, the ripening onset time was determined using a unified criterion based on the sustained shrinkage of one bubble and growth of the other, with transient fluctuations excluded by requiring persistent net molecular transfer over a finite time window. The detailed definition is provided in the SI. To facilitate a direct comparison among systems, we synchronized the trajectories by setting this onset point as time zero ($t = 0$) in later analysis. Figure 3a,b illustrate the temporal evolution of the relative sizes of both bubbles, averaged over all independent ripening trajectories for different systems. The results indicate that the dissolution of the small bubble is fastest in the acidic system, followed by the alkaline system (which is slightly faster than pure water), and slowest in the saline system. This evolution is clearly visualized by the representative snapshots in Figure 3c, selected from a single representative trajectory.

In addition, the apparent effective diffusion coefficient (D_{eff}) of N_2 molecules was calculated to describe the overall gas mobility in the double-bubble systems (detailed in the SI). As shown in Figure S9, the obtained D_{eff} follows the same trend as the ripening rate, implying that the observed ripening dynamics can be rationalized from the perspective of classical

https://doi.org/10.1021/jacs.6c08865
J. Am. Chem. Soc. 2026, 148, 32412−32425

diffusion-controlled gas transport, although it is beyond the present work.

The dissolution of the small bubble exhibits a pattern reminiscent of the single-bubble system. Moreover, the relative stability trend of single bubbles (Figure S10a) is consistent with the resistance ability of the smaller bubble to dissolution during the ripening process (Figure 3a), indicating that the ion-dependent single-bubble stability provides a useful baseline for interpreting the ripening dynamics of double bubbles.

Furthermore, the growth of the large bubble exhibits a distinct kinetic behavior from that of the small bubble. As demarcated by the vertical dashed lines in Figure 3a,b, the growth process of the large bubble is divided into pre- and postextinction stages of the small bubble. Prior to extinction of the small bubble, the large bubble in the saline system exhibits the slowest growth, while the other three systems are comparable. Following the extinction of the small bubble, the growth of large bubbles in all systems accelerates significantly until their sizes stabilize. The quantitative description of the above process is illustrated in Figure S11.

3.2. Interfacial Ion Distribution and Orientational Ordering

To further elucidate the microscopic mechanisms underlying the system-dependent bubble ripening behavior, we calculated the radial distribution of the ion concentration within the double-bubble systems. These profiles were determined relative to the Gibbs dividing surface (GDS) of the nanobubble, which is defined as the approximate location where the radial water density drops to half of the bulk value. To better describe the interfacial region, a relative normal distance from the GDS is defined as d_r, where $d_r < 0$ represents the region extending outward into the bulk phase, and $d_r > 0$ represents the inward gas phase. As shown in Figure 4, in acidic and alkaline systems, H_3O^+ and OH^- exhibit a stronger tendency to accumulate at the interface compared to their respective counterions. Qualitatively consistent with our previous findings,[65] the distribution peak of H_3O^+ is located closer to the GDS and exhibits a more localized profile compared to that of OH^- (see Figure S12).

In the saline system, a slightly stronger enrichment of Na^+ than Cl^- was observed in the subsurface region, deviating from existing reports for air–water interfaces, which proposed a preferential subsurface accumulation of Cl^-[78,79] or a colocalization of both ions within the same subsurface layer.[80,81] We attribute the inversion to the unique electrostatics of high-curvature nanobubbles. As detailed in Figure S13, the peak magnitude of the negative surface charge density is positively correlated with the bubble curvature (i.e., it increases significantly as the bubble size decreases). In particular, the specific orientation of water at the highly curved nanobubble boundary in this work leads to a substantial negative surface charge density (peaking at $\sim -0.5e/nm^3$, see Figure S10c). This intense electrostatic field may exert a strong enthalpic pull on cations, effectively overriding the subtle intrinsic interface affinity of Cl^-.[82] Consequently, Na^+ is electrostatically recruited to the interface, a mechanism analogous to the cation adsorption observed at negatively charged solid–liquid interfaces.[83−85]

Building upon these ionic distributions, we next evaluated the local net charge-density profiles near the nanobubble interface, which are also shown in Figure 4. The acidic and alkaline systems exhibit positive and negative charge-density peaks near the GDS, respectively, reflecting the local

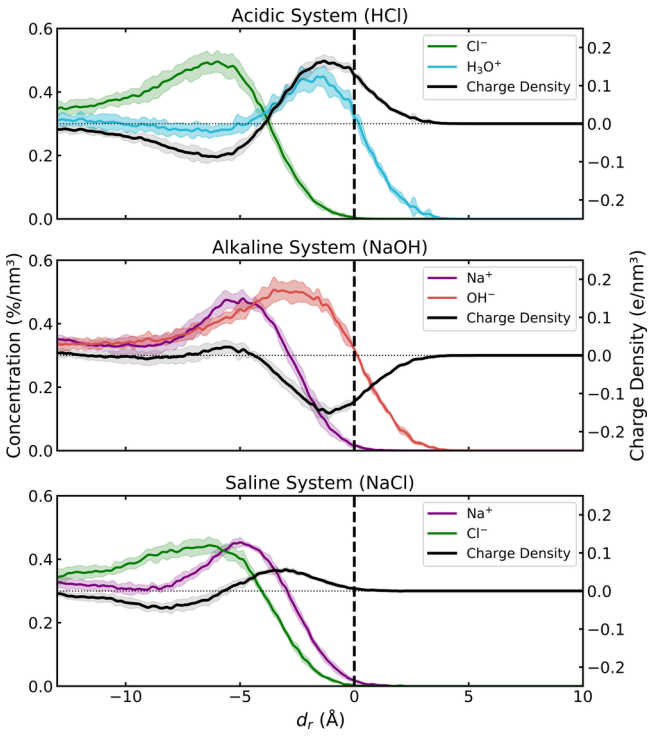

Figure 4. Ion concentration and local charge density profiles across the interface for acidic, alkaline, and saline systems. The solid curves represent the mean values calculated from three independent ripening trajectories for each system. The semitransparent shaded regions indicate the standard deviation. The vertical dashed line marks the location of the Gibbs dividing surface (GDS). The left and right y-axes correspond to the normalized ion number density and net charge density, respectively.

enrichment of H_3O^+ and OH^-. The signs of these charge density peaks are consistent with the experimentally reported zeta potentials of nanobubbles in acidic and alkaline solutions,[86] although such microscopic charge distribution should not be directly equated with the zeta potential defined at the slipping plane. In the saline system, Na^+ enrichment gives rise to a weak positive charge-density peak near the interface, whereas experimental zeta potentials are often negative.[86] This difference highlights the distinction between local ionic accumulation near the GDS and the macroscopic electrokinetic response.

Moving beyond ion distributions, we further probed how counterions modulate orientational ordering at the interface. Given that water molecules are the predominant interfacial species, we first calculated the radial profile of their average dipole orientation angle (θ_w, defined as the angle between the molecular dipole vector and the normal vector of the interface toward the bubble center as shown in Figure 5a) in all systems (Figure S15a). By comparing the results of simulation systems with and without counterions, we found that counterions drastically influence the orientation of interfacial water. In particular, they reverse the relative magnitudes of average θ_w in the acidic and alkaline systems, underscoring their important role in dictating interfacial structure. However, this average angle merely reflects the collective alignment of the interfacial water, obscuring the statistical distribution of molecular configurations. To transcend the limitation, in addition to θ_w, a twist angle φ which is defined as the azimuthal rotation of the water molecule around its dipole axis (Figure 5a), was also

https://doi.org/10.1021/jacs.6c08865
J. Am. Chem. Soc. 2026, 148, 32412−32425

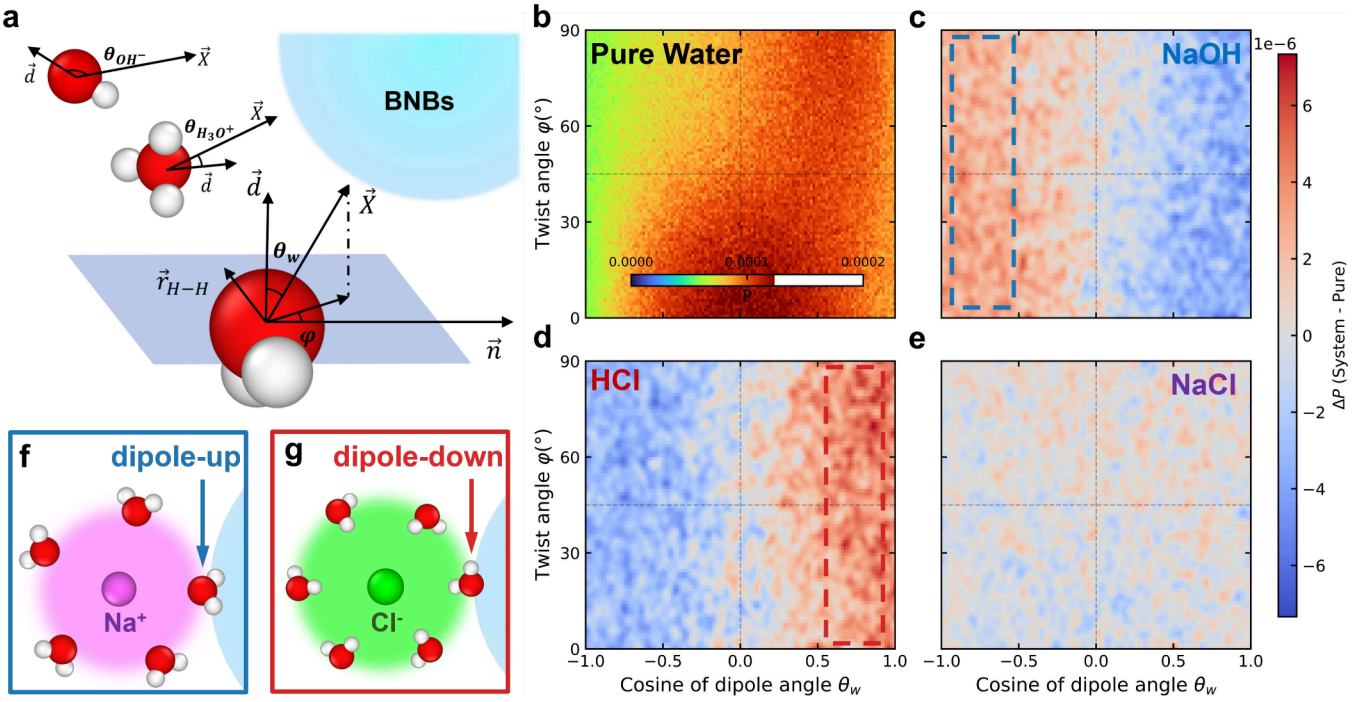

Figure 5. Definitions of orientational angles and comparative analysis of interfacial water configurations across different electrolyte systems. (a) Schematic definition of molecular and ionic orientational angles. The vector $\vec{d}$ is the dipole vector of the water molecules and ions. The vector $\vec{X}$ denotes the interface normal pointing toward the bubble center. For ions, θ_{OH^-} and $\theta_{H_3O^+}$ represent the dipole orientation angle of hydroxide and hydronium ions, respectively. For water molecules, θ_w represents the dipole orientation angle. The twist angle φ characterizes the molecular rotation around $\vec{d}$, measured as the angle between the molecular normal $\vec{n}$ and the projection of $\vec{X}$ onto the plane spanned by the interhydrogen vector $\vec{r}_{H-H}$ and $\vec{n}$. (b) Normalized probability heatmap showing the distribution of water molecule orientation, defined by the twist angle φ and cosine of dipole angle θ_w, in the pure water system. (c)−(e) Differential heatmaps revealing orientation variance in (c) alkaline, (d) acidic, and (e) saline systems relative to the pure water baseline shown in (b). (f)−(g) Schematics of hydration shells for (f) Na^+ and (g) Cl^- near the interface. The interfacial water molecules within these shells exhibit specific orientational configurations corresponding to those highlighted by the blue and red dashed boxes in (c) and (d), respectively. Panels (b)−(e) were calculated from three independent ripening trajectories for each system.

counted to map the configurational landscape of interfacial water, as used by Jedlovszky et al.[87]

A configurational baseline was established by plotting the joint probability distribution heatmap of θ_w and φ for the pure water system within the proximal interfacial region (PIR), defined by -2.5 Å $\leq d_r \leq 2.5$ Å. Figure 5b reveals the distribution of orientational alignment of interfacial water molecules with a nonuniform landscape characterized by distinct preferences for specific configurations (further details refer to the SI), in which the dominant configuration adopts an orientation parallel to the interface, consistent with previous reports.[88,89]

Subsequently, to isolate the structural perturbations induced by different electrolytes, difference heatmaps relative to the pure water baseline were constructed. The difference heatmaps (Figure 5c,d) show distinct system-dependent variations: the dipole-down configuration (dipole pointing toward the gas phase) is markedly suppressed in the alkaline system, whereas the dipole-up configuration (dipole pointing toward the bulk water region) is promoted; the acidic system exhibits an opposite trend. This divergence may be attributed to the hydration structural constraints imposed by counterions, as schematically illustrated in Figure 5f,g. Further analyses presented in Figure S16 show that Na^+ and OH^- exert opposite effects on interfacial water orientation in the alkaline system, qualitatively consistent with recent heterodyne-detected vibrational sum-frequency generation (HD-VSFG) observations.[80] Notably, the configurational profile of the saline system is virtually indistinguishable from that of pure water (Figure 5e), indicating that the impact of Na^+ and Cl^- on the orientation of interfacial water may offset each other. This weak perturbation is also qualitatively consistent with recent HD-VSFG measurements.[80]

Shifting focus from water to ions, we defined the dipole orientation angle $\theta_{OH^-}/\theta_{H_3O^+}$ for OH^-/H_3O^+ as the angle between the ionic dipole vector and the vector pointing from the oxygen atom toward the bubble center (Figure 5a). Based on this definition, the radial profiles of their average dipole orientation angles were calculated to evaluate their interfacial alignment (Figure S15b). Interestingly, both species display distinct intrinsic orientation preferences at the interface from those in the bulk phase, becoming more ordered (with the averaged $\theta_{OH^-}/\theta_{H_3O^+}$ deviating from 90°). Despite this pronounced interfacial ordering, their orientations remain insensitive to the presence of counterions. The only marginal enhancement observed can be ascribed to minor ion-dipole interactions between counterions and OH^-/H_3O^+.

3.3. Interfacial Hydrogen Bond and Na^+–Cl^- Coupling Analysis

Given that the alignment of interfacial water and OH^-/H_3O^+ may affect the HB network, we proceeded to examine its detailed characteristics within the PIR. First, a persistent HB asymmetry of interfacial water molecules was observed in all

https://doi.org/10.1021/jacs.6c08865
J. Am. Chem. Soc. 2026, 148, 32412−32425

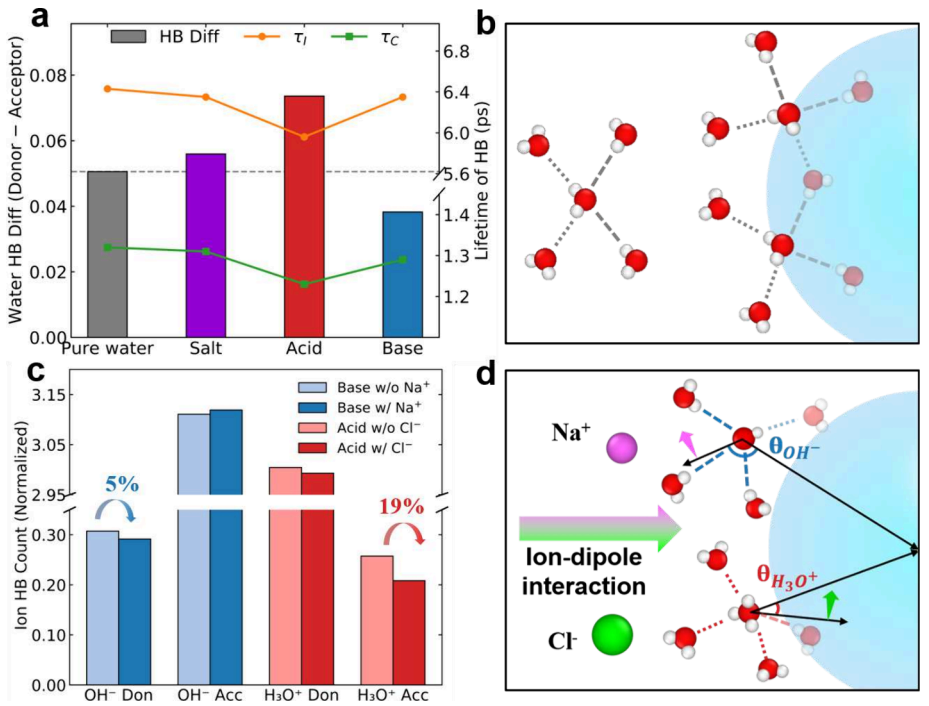

Figure 6. Hydrogen bond (HB) characteristics of interfacial water and ions across different systems. (a) HB analysis of interfacial water molecules. The bar chart represents the difference between the normalized donor and acceptor HB counts. The orange and green lines indicate the intermittent and continuous HB lifetimes, respectively. (b) Schematic illustration demonstrating the relationship between HB asymmetry and the orientation of interfacial water molecules. (c) Comparison of the normalized donor and acceptor HB counts for H_3O^+ and OH^- ions in acidic and alkaline systems, respectively, evaluated in the presence and absence of their corresponding counterions. "Don" and "Acc" denote the donor and acceptor HB, respectively. The curved arrows and percentages highlight the relative reduction in HB counts upon the introduction of counterions. (d) Schematic illustration of the mechanism by which counterions enhance the orientational preferences of H_3O^+ and OH^- near the interface, thereby attenuating the HB connectivity on their respective gas-facing sides. In the schematic representations, the purple/green pointed-tail arrow in (d) denotes the enlarged/reduced orientation angle of OH^-/H_3O^+ near the interface due to counterions. The dotted and dashed lines denote donor and acceptor HBs, respectively. The colors of dotted and dashed lines distinguish the specific species forming HBs with surrounding water molecules: gray for water, blue for OH^-, and red for H_3O^+. The transparent water molecules and HBs indicate weakened HB connectivity. Panels (a) and (c) were calculated from three independent ripening trajectories for each corresponding system.

systems, characterized by a slight excess in the normalized number of HB donors over acceptors. Crucially, this HB asymmetry inherently reflects topological defects within the HB network, which closely govern the thermodynamic and dynamic stability of the HB network. Figure 6a shows that, relative to the pure water baseline, the HB asymmetry is enhanced in the acidic system and weakened in the alkaline system. Although the magnitude of this asymmetry is system-dependent, the HB asymmetry in the saline system is closer to that of pure water. Further analysis reveals an obvious correlation between the degree of HB asymmetry and the orientation preference of interfacial water: a higher degree of HB asymmetry corresponds to a configuration profile of more dipole-down water molecules (Figure 5b,d), implying that the HB-network topology is intrinsically coupled to the alignment of interfacial water (Figure 6b).

Additionally, the lifetime of HB was calculated to evaluate the dynamics of interfacial water−water HB network using the time correlation function:[90,91]

$$C_{HB}(t) = \frac{\langle h_{ij}(0)\cdot h_{ij}(t)\rangle_{\Delta t}}{\langle h_{ij}(0)^2\rangle} \quad (1)$$

$$\tau = \int_0^\infty C_{HB}(t)\,dt \quad (2)$$

where $h_{ij}(t)$ is a binary population variable denoting the HB state between molecules i and j at time t ($h_{ij}(t) = 1$ if the HB is intact and 0 otherwise, $h_{ij}(0)$ is $h_{ij}(t)$ at $t = 0$), and the angular brackets $\langle ... \rangle$ represent the ensemble average. Depending on the tolerance time (Δt) allowed for transient breakages, two types of HB lifetime are evaluated: the continuous lifetime (τ_C with $\Delta t = 0$) and the intermittent lifetime (τ_I with $\Delta t = \infty$). More details are provided in the SI. The calculated values for both types of HB lifetime are presented as line plots in Figure 6a. Compared to the pure water system, the continuous and intermittent lifetimes in both alkaline and saline systems remain nearly unchanged, whereas those in the acidic system exhibit a substantial decrease.

In summary, the obtained asymmetry and lifetime of interfacial water−water HBs reveal a distinct system-dependent variation of the interfacial HB network. Compared to the pure water system, the acidic system exhibits pronounced HB asymmetry and shortened lifetime, collectively signifying a severely weakened interfacial HB network. The saline system displays nearly unchanged structural asymmetry and HB lifetime comparable to those of pure water, reflecting a well-preserved, pure-water-like HB network. In contrast, the alkaline system suppresses the asymmetry of HB while preserving the intrinsic HB lifetime, ultimately yielding a stabilized and enhanced interfacial HB network.

https://doi.org/10.1021/jacs.6c08865
J. Am. Chem. Soc. 2026, 148, 32412−32425

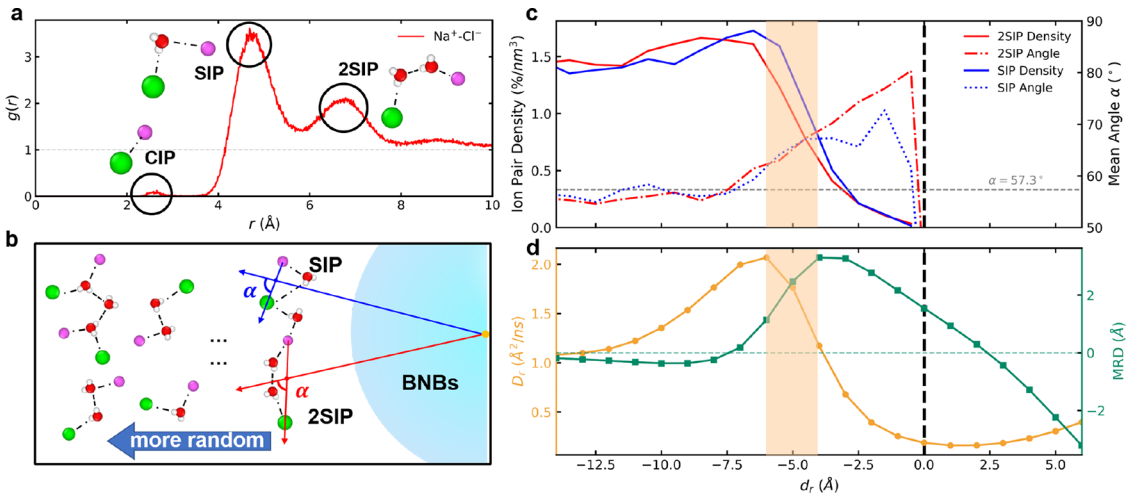

Figure 7. Analysis of ion pairs and the radial diffusion dynamics of nitrogen molecules in the saline system. (a) Radial distribution function, $g(r)$, of Na^+-Cl^- pairs, where distinct peaks identify three ion-pairing modes: contact ion pair (CIP), solvent-separated ion pair (SIP), and double solvent-separated ion pair (2SIP). (b) Schematic illustration of SIP and 2SIP configurations near the gas−liquid interface, defining the orientation angle α relative to the radial vector. In panels (a) and (b), purple and green spheres represent Na^+ and Cl^- ions, respectively. (c) Radial profiles showing the normalized number density and mean orientation angle of SIP and 2SIP as a function of distance from the interface. The gray horizontal dashed line denotes the spatial average orientation angle α of 57.3° that exhibits randomly oriented ion pairs in the bulk water region. (d) Spatially resolved dynamics of nitrogen molecules, characterized by the radial diffusion coefficient (D_r) and mean radial displacement (MRD) of nitrogen molecules near the interface. The vertical dashed lines in (c) and (d) denote the position of the GDS. Panels (c) and (d) were calculated from three independent ripening trajectories in the saline system.

For interfacial H_3O^+/OH^--involved HBs, we found that counterions attenuate the role of OH^- as an HB donor and the role of H_3O^+ as an HB acceptor (Figure 6c), which is fundamentally governed by the ion-dipole interactions mentioned earlier. These interactions enhance the orientational preferences of both ions at the interface by directing the hydrogen atom of OH^- and the oxygen atom of H_3O^+ more predominantly toward the gas-facing side. This alignment imposes greater steric hindrance, restricting their participation as an HB donor and acceptor respectively, as schematically illustrated in Figure 6d. Although these interactions exert only a marginal influence on the orientation of OH^- and H_3O^+, this subtle perturbation geometrically restricts HBs of the gas-facing side, leading to a diminished HB connectivity.

Fundamentally, the ripening of nanobubbles is governed by the diffusion of gas molecules across the interfacial water layer. As illustrated in our previous work,[65] this process is thermodynamically modulated by two factors: the orientational alignment of interfacial water that dictates the entropic effect and the properties of interfacial HBs that govern the enthalpic barrier. Through this thermodynamic perspective, the analyses presented thus far reveal a striking anomaly for the saline system. Compared to the pure water system, the saline system exhibits nearly indistinguishable interfacial water alignment and HB asymmetry, along with a comparable HB lifetime. Therefore, how can the significantly slower nanobubble ripening rate in the saline system compared to that in the pure water system be rationalized thermodynamically? To resolve this apparent discrepancy, we further investigated the interactions between Na^+ and Cl^- ions near the interface in the saline system.

Although the interfacial profiles indicate that the distributions of Na^+ and Cl^- ions are in close spatial proximity along the radial direction of the bubble (Figure 4), the Na^+-Cl^- RDF reveals a dominant peak at ~4.5 Å rather than a short-range peak (Figure 7a). These complementary spatial distributions suggest that Na^+ and Cl^- ions may adopt specific configurations near the interface. To quantitatively analyze, based on the Na^+-Cl^- RDF, we identified three distinct interaction modes: contact ion pairs (CIPs), solvent-shared ion pairs (SIPs), and double solvent-separated ion pairs (2SIPs). More details of this categorization are provided in the SI. As the population of CIPs is negligible compared to that of SIPs and 2SIPs as shown in Figure 7a, our subsequent analysis focuses exclusively on the latter two types.

Considering that the orientation of ion pairs can reshape the hydration structure near the interface, an ion-pair orientation angle α was defined as the acute angle between the dipole vector of the ion pair and the normal vector of the interface passing through the midpoint of the line connecting the Na^+ and Cl^- ions (Figure 7b). The radial profiles of mean α shown in Figure 7c reveal distinct spatially dependent behaviors. Within the proximal aqueous layer (-4 Å $\leq d_r \leq 0$ Å), the mean orientation angles are mostly between 70° and 80°, indicating a preferential orientation that is tangential to the interface (hereafter denoted as "lying-flat" configuration). As the distance extends deeper into the bulk phase, this ordered alignment gradually relaxes, with the mean α converging to 57.3° (the mean angle for random orientation; derivation in the SI). In tandem with this structural randomization, the density of ion pairs undergoes a sharp surge within the aqueous layer (-6 Å $\leq d_r \leq -4$ Å), after which it maintains a stable plateau in the bulk phase.

These concurrent structural features, namely, the dense accumulation of ion pairs and their "lying-flat" configuration, may have profound implications for gas transport. A previous study by Feng et al. suggested that ionic hydration shells impede gas diffusion,[37] an effect presumably intensified by the dense accumulation of these specific orientational configurations. We hypothesize that this synergistic structural arrangement promotes the emergence of localized and rigid hydration layers, which significantly restrict gas diffusion.

https://doi.org/10.1021/jacs.6c08865
J. Am. Chem. Soc. 2026, 148, 32412−32425

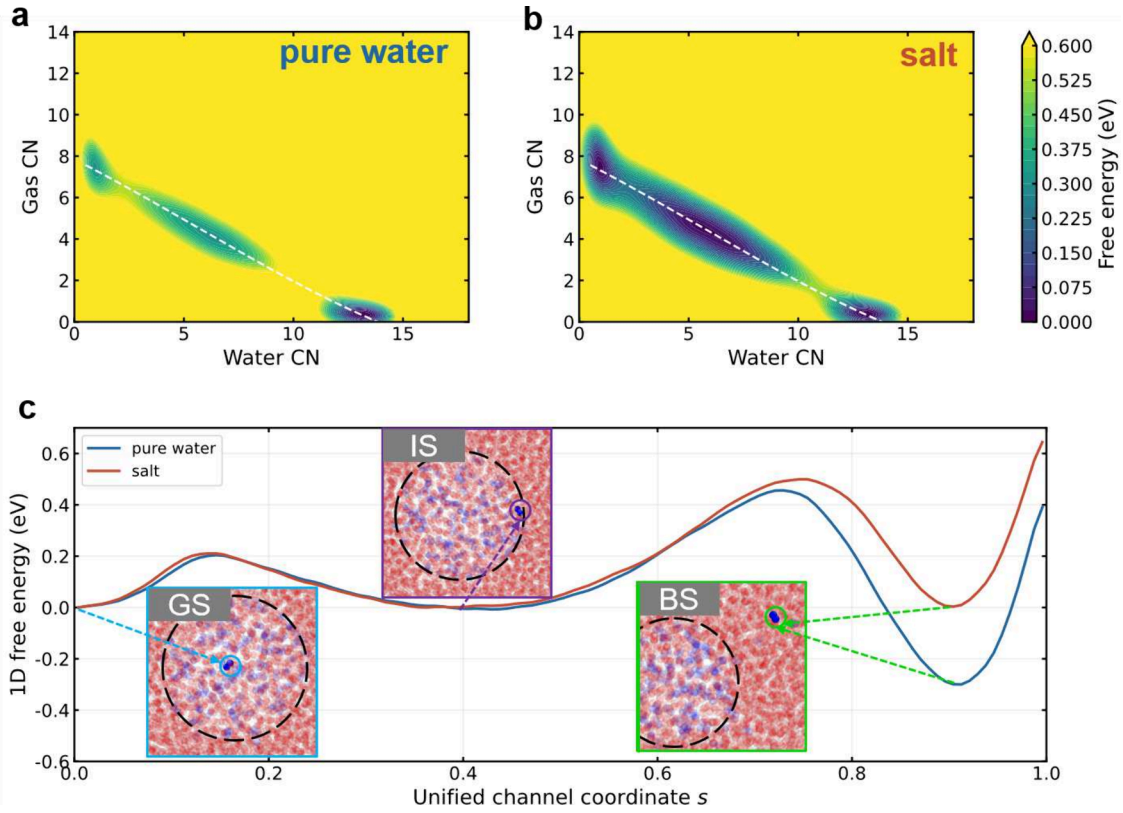

Figure 8. Free-energy profiles of N2 transfer from the nanobubble to the bulk region. Two-dimensional free-energy surfaces as functions of the gas coordination number (Gas CN) and water coordination number (Water CN) for (a) pure water and (b) the saline system. The white dashed lines indicate the gas-to-bulk transition channels used for the one-dimensional projection. (c) One-dimensional free-energy profiles projected along the unified channel coordinate s, defined as the path coordinate along the common transition channel of both systems scaled from 0 to 1. The insets show representative configurations of the probe N_2 molecule in the gas state (GS), interfacial state (IS), and bulk state (BS). The black dashed circles mark the nanobubble, and molecules other than the probe N_2 molecule are shown with reduced opacity for clarity.

To verify this hypothesis and quantitatively characterize the diffusion dynamics of nitrogen molecules, we calculated the radial diffusion coefficient (D_r) and the mean radial displacement (MRD) of N_2 molecules using a 5 Å-thick radial moving window with a 1 Å sliding step relative to the instantaneous gas−liquid interface. The obtained values of D_r and MRD were ensemble-averaged over multiple N_2 molecules and time origins within the selected ripening trajectories; further details are provided in the SI. The results reveal a pronounced increase in the diffusion coefficient around $d_r = -5$ Å (i.e., the light orange shaded region in Figure 7d). Meanwhile, the MRD decreases markedly in this region, indicating that the outward radial migration of N_2 molecules is substantially suppressed once they approach this region. Since bubble ripening relies on gas transfer from the nanobubble into the surrounding solution, this resistance region contributes to the slower ripening rate in the saline system.

More importantly, the spatial span of this dynamic resistance region (-6.0 Å $\leq d_r \leq -4.0$ Å), indicated by the increase of D_r and the decrease of the MRD, coincides precisely with the region of localized enrichment of "lying-flat" ion pairs ($\alpha \sim 60°-70°$), as highlighted by the light orange shaded region in Figure 7c,d. This spatial congruence strongly corroborates our hypothesis: the accumulation of "lying-flat" solvent-separated ion pairs near the interface forms a robust barrier by hydration interaction that effectively intercepts the diffusion of gas molecules. Consistently, the low-concentration NaCl system (0.056 M) exhibits a shorter dissolution time than the regular NaCl system (0.22 M) but remains slower than the acidic, alkaline, and pure water systems (Figure S7b), indicating that weakening the salt concentration reduces but does not eliminate the retardation effect. Moreover, NaCl slightly increases the diffusion coefficient of dissolved N_2 in bulk solution compared with pure water, whereas it decreases the apparent effective diffusion coefficient in nanobubble systems (Figure S17). This opposite trend further supports that the slowed gas transport in the saline nanobubble system originates from interface-induced ion-pair hydration structures rather than from a simple reduction of bulk N_2 diffusivity by salt.

3.4. Ion-Regulated Nanobubble Ripening Mechanism

Based on the evolution dynamics simulation results of double nanobubbles and the comprehensive structural and dynamic insights established above, we propose an ion-regulated bubble ripening mechanism. Within this framework, the hydration effect of counterions modulates the orientational alignment of interfacial water, thereby influencing the asymmetry of interfacial water−water HBs. Concurrently, the electrostatic effect of counterions reinforces orientational preferences of OH^- and H_3O^+ at the interface, attenuating their HB connectivity on the gas-facing side. Furthermore, the specific coupling of Na^+ and Cl^- ions promotes the formation of dense hydration layers near the interface. These ion-regulated structural alterations dictate the relative dominance of entropic and enthalpic contributions, which thermodynamically controls the diffusion of gas molecules, as elaborated below.

https://doi.org/10.1021/jacs.6c08865
J. Am. Chem. Soc. 2026, 148, 32412−32425

From an entropic perspective, the different ripening dynamics can be associated with the distinct ordering of interfacial water. Compared to the pure water system, the acidic system exhibits a higher degree of orientational order of interfacial water (Figure 5b,d), corresponding to a low-entropy state. Disruption of this relatively ordered interfacial water shell by gas molecules may provide an entropic driving force for gas diffusion. In contrast, the highly disordered interfacial water in the alkaline system (Figure 5b,c) and the pure-water-like orientation in the saline system (Figure 5b,e) correspond to relatively higher entropy states. Consequently, these two systems have no additional entropic advantage, exerting negligible influence on gas diffusion.

The enthalpic landscape, mainly reflected by interfacial HB structures and ion-pair coupling, presents an even more complex competitive scenario. In the acidic system, a structurally and dynamically fragile HB network, evidenced by pronounced HB asymmetry and shortened lifetime, is further weakened by the attenuated hydrogen bonding of H_3O^+ on the gas-facing side. This combined lability reduces the enthalpic barrier to gas diffusion. In the alkaline system, the enthalpic contributions exhibit internal cancellations: the enhanced stability of the water−water HB network (nearly unchanged lifetime and reduced asymmetry) is effectively offset by the weakened hydrogen bonding of OH^- on the gas-facing side. In contrast, the saline system features a preserved pure-water-like HB network (nearly unchanged asymmetry and lifetime). The specific coupling of Na^+ and Cl^- ions facilitates the formation of solvent-separated ion pairs and dense hydration layers near the interface, promoting an enthalpic barrier that hinders gas transport.

Ultimately, the ripening processes are strongly rationalized by these distinct thermodynamic balances. The acidic system benefits from a synergistic combination of a strong entropic driving force and a reduced enthalpic barrier for diffusion of nitrogen molecules, thereby accelerating the ripening process. The alkaline system, characterized by a marginal entropic effect and an internally canceled enthalpy, displays a ripening rate nearly identical to that of pure water. Finally, the saline system features a similarly marginal entropic effect, leaving an overwhelming enthalpic barrier imposed by the coupling of ion pairs to act as the mechanism that substantially retards the ripening process.

To further support this interpretation, we performed enhanced-sampling calculations for representative pure water and saline systems to obtain the free-energy profiles of N_2 transfer from the nanobubble to the bulk region (Figure 8). Compared with pure water, the saline system exhibits a higher free-energy barrier and a less negative free-energy change for N_2 transfer from the interface to the bulk phase, indicating that gas transfer into the bulk phase is both kinetically more hindered and thermodynamically less favored. These free-energy results provide direct thermodynamic support for the proposed salt-retarded ripening mechanism.

It should be noted that the present simulations focus on BNBs with an initial radius of approximately 1.5 nm. The ripening kinetics are expected to be size-dependent because of curvature effects. Therefore, the present mechanism should be interpreted primarily for highly curved BNBs of comparable size.

4. CONCLUSIONS

In summary, leveraging a high-accuracy NEP89 model fine-tuned for gas−electrolyte interfaces, we performed efficient GPUMD simulations to investigate the Ostwald ripening process of bulk nanobubbles in acidic, alkaline, and saline systems, with a specific focus on the role of counterions.

By quantifying the interfacial water orientation using a pair of orientational coordinates, we revealed that counterions significantly modulate water alignment through local hydration effects. This structural perturbation intrinsically dictates the interfacial configurational entropy and the asymmetry of the interfacial HB network. Besides, counterions slightly enhance the orientational preference of H_3O^+ and OH^- ions near the interface via electrostatic effects, further attenuating the specific HB connectivity on gas-facing sides. Compared to pure water, the interfacial water−water HB lifetime remains stable in the alkaline and saline systems but is significantly shortened in the acidic system. By analyzing the ion pairs and radial gas diffusion in the saline system, a Na^+−Cl^- coupling mechanism was elucidated. Specifically, we uncovered a localized enrichment of "lying-flat" ion pairs within a specific bulk water region near the interface. These specific configurations form dense interfacial hydration layers that retard radial diffusion of gas molecules.

Based on the detailed analyses aforementioned, we elucidate an ion-regulated ripening mechanism governed by the relative dominance of entropic and enthalpic contributions. Synergistic entropic-enthalpic advantages accelerate ripening in the acidic system, whereas internal enthalpic cancellations render the ripening rate of the alkaline system virtually identical to that of pure water. Most notably, the remarkable resistance to ripening in the saline system is caused by a dominant enthalpic barrier, arising from the coupling of the Na^+ and Cl^- ions. This salt-retarded mechanism is further supported by free-energy profiles obtained from enhanced-sampling molecular dynamics simulations, which reveal a higher barrier for N_2 transfer from the nanobubble to the bulk phase in the saline system.

The current work provides an atomistic physicochemical framework of bulk nanobubble ripening modulated by interfacial ions. Looking ahead, we plan to train a more robust machine learning potential that incorporates explicit charge interactions and external electric fields. These advancements will allow us to simulate more realistic application scenarios, further elucidating the dynamical behavior of electrochemical nanobubbles at the atomic scale.

■ ASSOCIATED CONTENT

Data Availability Statement

The data that support the findings of this study are available in the Supporting Information of this article. This includes NEP model training, data set building, and other computational details. The simulation and visualization software packages employed for performing the calculations are freely accessible. The necessary input files for replicating the research can be obtained at https://github.com/Guo-xiangd/Bibubble_ripening.

Supporting Information

The Supporting Information is available free of charge at https://pubs.acs.org/doi/10.1021/jacs.6c08865.

Details of potential model generation, including DP-GEN-based data set construction, DFT calculations, DP

https://doi.org/10.1021/jacs.6c08865
J. Am. Chem. Soc. 2026, 148, 32412−32425

model training, and NEP89 fine-tuning; molecular dynamics simulation details and single-nanobubble evolution in different systems; methodological details, including the construction of Markov transition probability matrices, definition of ripening onset time and dissolution-time analysis, calculation of N_2 diffusion coefficients, enhanced sampling settings with the employed collective variables, and free energy calculations; additional analysis protocols, including interfacial water orientation, interfacial hydrogen-bond lifetime, cluster cutoff selection, identification of ionic species, hydrogen-bond criteria, and surface-energy calculations (PDF)

AUTHOR INFORMATION

Corresponding Authors

Pengchao Zhang − *Center for Combustion Energy, Department of Energy and Power Engineering, and Key Laboratory for Thermal Science and Power Engineering of Ministry of Education, Tsinghua University, Beijing 100084, China; New Cornerstone Science Laboratory, Tsinghua University, Beijing 100084, China;* orcid.org/0000-0002-6556-6588; Email: zhangpengchao@tsinghua.edu.cn

Chao Sun − *Center for Combustion Energy, Department of Energy and Power Engineering, and Key Laboratory for Thermal Science and Power Engineering of Ministry of Education, Tsinghua University, Beijing 100084, China; New Cornerstone Science Laboratory and Department of Engineering Mechanics, School of Aerospace Engineering, Tsinghua University, Beijing 100084, China;* orcid.org/0000-0002-0930-6343; Email: chaosun@tsinghua.edu.cn

Xuefei Xu − *Center for Combustion Energy, Department of Energy and Power Engineering, and Key Laboratory for Thermal Science and Power Engineering of Ministry of Education, Tsinghua University, Beijing 100084, China;* orcid.org/0000-0002-2009-0483; Email: xuxuefei@tsinghua.edu.cn

Author

Xiangdang Guo − *Center for Combustion Energy, Department of Energy and Power Engineering, and Key Laboratory for Thermal Science and Power Engineering of Ministry of Education, Tsinghua University, Beijing 100084, China;* orcid.org/0009-0002-8910-7359

Complete contact information is available at: https://pubs.acs.org/10.1021/jacs.6c08865

Notes

The authors declare no competing financial interest.

ACKNOWLEDGMENTS

This work received partial support from the National Natural Science Foundation of China (Grant Nos. 22473066 and 12588201), the Creative Seed Fund of Shanxi Research Institute for Clean Energy of Tsinghua University, and the Shui Mu Scholarship at Tsinghua University (2025SM043). Computational resources were partially supported by the Open Source Supercomputing Center of S-A-I.

REFERENCES

(1) Li, C.; Zhang, H. A Review of Bulk Nanobubbles and Their Roles in Flotation of Fine Particles. *Powder Technol.* **2022**, *395*, 618−633.

(2) Azevedo, A.; Oliveira, H.; Rubio, J. Bulk Nanobubbles in the Mineral and Environmental Areas: Updating Research and Applications. *Adv. Colloid Interface Sci.* **2019**, *271*, 101992.

(3) Tao, D. Recent Advances in Fundamentals and Applications of Nanobubble Enhanced Froth Flotation: A Review. *Miner. Eng.* **2022**, *183*, 107554.

(4) Xiao, W.; Zhang, H.; Wang, X.; Wang, B.; Long, T.; Deng, S.; Yang, W. Interaction Mechanisms and Application of Ozone Micro/Nanobubbles and Nanoparticles: A Review and Perspective. *Nanomaterials* **2022**, *12*, 1958.

(5) Yu, W.; Chen, J.; Ateia, M.; Cates, E. L.; Johnson, M. S. Do Gas Nanobubbles Enhance Aqueous Photocatalysis? Experiment and Analysis of Mechanism. *Catalysts* **2021**, *11*, 511.

(6) Babu, K. S.; Amamcharla, J. K. Generation Methods, Stability, Detection Techniques, and Applications of Bulk Nanobubbles in Agro-Food Industries: A Review and Future Perspective. *Crit. Rev. Food Sci. Nutr.* **2023**, *63*, 9262−9281.

(7) Yasuda, K. Characteristics of Ultrafine Bubbles (Bulk Nanobubbles) and Their Application to Particle-Related Technology. *KONA Powder Part. J.* **2024**, *41*, 183−196.

(8) Patel, A. K.; Singhania, R. R.; Chen, C.-W.; Tseng, Y.-S.; Kuo, C.-H.; Wu, C.-H.; Dong, C. D. Advances in Micro- and Nano Bubbles Technology for Application in Biochemical Processes. *Environ. Technol. Innov.* **2021**, *23*, 101729.

(9) Paknahad, A. A.; Kerr, L.; Wong, D. A.; Kolios, M. C.; Tsai, S. S. Biomedical Nanobubbles and Opportunities for Microfluidics. *RSC Adv.* **2021**, *11*, 32750−32774.

(10) Hansen, H. H.; Cha, H.; Ouyang, L.; Zhang, J.; Jin, B.; Stratton, H.; Nguyen, N.-T.; An, H. Nanobubble Technologies: Applications in Therapy from Molecular to Cellular Level. *Biotechnol. Adv.* **2023**, *63*, 108091.

(11) Fox, F. E.; Herzfeld, K. F. Gas Bubbles With Organic Skin as Cavitation Nuclei. *J. Acoust. Soc. Am.* **1954**, *26*, 984−989.

(12) Zhang, X.; Liu, X.; Zhong, Y.; Zhou, Z.; Huang, Y.; Sun, C. Q. Nanobubble Skin Supersolidity. *Langmuir* **2016**, *32*, 11321−11327.

(13) Weijs, J. H.; Seddon, J. R.; Lohse, D. Diffusive Shielding Stabilizes Bulk Nanobubble Clusters. *ChemPhysChem* **2012**, *13*, 2197−2204.

(14) Yurchenko, S. O.; Shkirin, A. V.; Ninham, B. W.; Sychev, A. A.; Babenko, V. A.; Penkov, N. V.; Kryuchkov, N. P.; Bunkin, N. F. Ion-Specific and Thermal Effects in the Stabilization of the Gas Nanobubble Phase in Bulk Aqueous Electrolyte Solutions. *Langmuir* **2016**, *32*, 11245−11255.

(15) Dockar, D.; Sullivan, P.; Mifsud, J.; Gibelli, L.; Borg, M. K. Ionic Adsorption on Bulk Nanobubble Interfaces and Its Uncertain Role in Diffusive Stability. *J. Colloid Interface Sci.* **2025**, *695*, 137747.

(16) Wang, S.; Zhou, L.; Wang, X.; Hu, J.; Li, P.; Lin, G.; Gao, Y.; Zhang, L.; Wang, C. Collective Dynamics of Bulk Nanobubbles With Size-Dependent Surface Tension. *Langmuir* **2021**, *37*, 7986−7994.

(17) Nirmalkar, N.; Pacek, A.; Barigou, M. On the Existence and Stability of Bulk Nanobubbles. *Langmuir* **2018**, *34*, 10964−10973.

(18) Bu, X.; Zhou, S.; Tian, X.; Ni, C.; Nazari, S.; Alheshibri, M. Effect of Aging Time, Airflow Rate, and Nonionic Surfactants on the Surface Tension of Bulk Nanobubbles Water. *J. Mol. Liq.* **2022**, *359*, 119274.

(19) Zhou, Y.; Han, Z.; He, C.; Feng, Q.; Wang, K.; Wang, Y.; Luo, N.; Dodbiba, G.; Wei, Y.; Otsuki, A.; Fujita, T. Long-Term Stability of Different Kinds of Gas Nanobubbles in Deionized and Salt Water. *Materials* **2021**, *14*, 1808.

(20) Wang, Q.; Zhao, H.; Qi, N.; Qin, Y.; Zhang, X.; Li, Y. Generation and Stability of Size-Adjustable Bulk Nanobubbles Based on Periodic Pressure Change. *Sci. Rep.* **2019**, *9*, 1118.

(21) Lee, J. I.; Huh, H. S.; Park, J. Y.; Han, J.-G.; Kim, J.-M. Coarsening Behavior of Bulk Nanobubbles in Water. *Sci. Rep.* **2021**, *11*, 19173.

(22) Ma, T.; Kimura, Y.; Yamamoto, H.; Feng, X.; Hirano-Iwata, A.; Niwano, M. Characterization of Bulk Nanobubbles Formed by Using a Porous Alumina Film With Ordered Nanopores. *J. Phys. Chem. B* **2020**, *124*, 5067−5072.
(23) Bird, E.; Zhou, J.; Liang, Z. Coalescence Speed of Two Equal-Sized Nanobubbles. *Phys. Fluids* **2020**, *32*, 123304.
(24) Bird, E.; Smith, E.; Liang, Z. Coalescence Characteristics of Bulk Nanobubbles in Water: A Molecular Dynamics Study Coupled With Theoretical Analysis. *Phys. Rev. Fluids* **2021**, *6*, 093604.
(25) Dixit, A. K.; Das, A. K. Molecular Approach for Understanding the Stability, Collision, and Coalescence of Bulk Nanobubbles. *Langmuir* **2022**, *38*, 16122−16133.
(26) Lu, Y.; Yang, L.; Kuang, Y.; Song, Y.; Zhao, J.; Sum, A. K. Molecular Simulations on the Stability and Dynamics of Bulk Nanobubbles in Aqueous Environments. *Phys. Chem. Chem. Phys.* **2021**, *23*, 27533−27542.
(27) Voorhees, P. W. The Theory of Ostwald Ripening. *J. Stat. Phys.* **1985**, *38*, 231−252.
(28) Smoluchowski, M. v. Versuch Einer Mathematischen Theorie Der Koagulationskinetik Kolloider Lösungen. *Z. Für Phys. Chem.* **1918**, *92U*, 129−168.
(29) Kaiser, S.; Plansky, J.; Krinninger, M.; Shavorskiy, A.; Zhu, S.; Heiz, U.; Esch, F.; Lechner, B. A. Does Cluster Encapsulation Inhibit Sintering? Stabilization of Size-Selected Pt Clusters on Fe_3O_4 (001) by SMSI. *ACS Catal.* **2023**, *13*, 6203−6213.
(30) Lai, K. C.; Evans, J. W. Complex Oscillatory Decrease With Size in Diffusivity of {100}-Epitaxially Supported 3D FCC Metal Nanoclusters. *Nanoscale* **2019**, *11*, 17506−17516.
(31) Liu, Y.; Kathan, K.; Saad, W.; Prud'homme, R. K. Ostwald Ripening of β-Carotene Nanoparticles. *Phys. Rev. Lett.* **2007**, *98*, 036102.
(32) Thompson, K. L.; Derry, M. J.; Hatton, F. L.; Armes, S. P. Long-Term Stability of N-Alkane-in-Water Pickering Nanoemulsions: Effect of Aqueous Solubility of Droplet Phase on Ostwald Ripening. *Langmuir* **2018**, *34*, 9289−9297.
(33) Inoue, S.; Kimura, Y.; Uematsu, Y. Ostwald Ripening of Aqueous Microbubble Solutions. *J. Chem. Phys.* **2022**, *157*, 244704.
(34) Uematsu, Y. Ostwald Ripening of Buoyancy-Driven Microbubbles. *J. Chem. Phys.* **2025**, *162*, 161102.
(35) Dollet, B.; Lohse, D. Pinning Stabilizes Neighboring Surface Nanobubbles Against Ostwald Ripening. *Langmuir* **2016**, *32*, 11335−11339.
(36) Zhu, X.; Verzicco, R.; Zhang, X.; Lohse, D. Diffusive Interaction of Multiple Surface Nanobubbles: Shrinkage, Growth, and Coarsening. *Soft Matter* **2018**, *14*, 2006−2014.
(37) Feng, M.; Ma, X.; Zhang, Z.; Luo, K. H.; Sun, C.; Xu, X. How Sodium Chloride Extends Lifetime of Bulk Nanobubbles in Water. *Soft Matter* **2022**, *18*, 2968−2978.
(38) Parsons, D. F.; Ninham, B. W. Surface Charge Reversal and Hydration Forces Explained by Ionic Dispersion Forces and Surface Hydration. *Colloids Surf. A: Physicochem. Eng. Asp.* **2011**, *383*, 2−9.
(39) Bunkin, N.; Shkirin, A. Nanobubble Clusters of Dissolved Gas in Aqueous Solutions of Electrolyte. II. Theoretical Interpretation. *J. Chem. Phys.* **2012**, *137*, 054707.
(40) Hammons, J. A.; Kang, S.; Ferron, T. J.; Aydin, F.; Lin, T. Y.; Seung, K.; Chow, P.; Xiao, Y.; Davis, J. T. Nanobubble Formation and Coverage During High Current Density Alkaline Water Electrolysis. *Nano Lett.* **2024**, *24*, 13695−13701.
(41) Wu, J.; Zhang, K.; Cen, C.; Wu, X.; Mao, R.; Zheng, Y. Role of Bulk Nanobubbles in Removing Organic Pollutants in Wastewater Treatment. *AMB Express* **2021**, *11*, 96.
(42) Nazari, S.; Hassanzadeh, A.; He, Y.; Khoshdast, H.; Kowalczuk, P. B. Recent Developments in Generation, Detection and Application of Nanobubbles in Flotation. *Minerals* **2022**, *12*, 462.
(43) Wang, X.; Li, P.; Ning, R.; Ratul, R.; Zhang, X.; Ma, J. Mechanisms on Stability of Bulk Nanobubble and Relevant Applications: A Review. *J. Clean. Prod.* **2023**, *426*, 139153.
(44) Zhou, L.; Wang, S.; Zhang, L.; Hu, J. Generation and Stability of Bulk Nanobubbles: A Review and Perspective. *Curr. Opin. Colloid Interface Sci.* **2021**, *53*, 101439.
(45) Li, J.; Zhang, H.; Guo, Z.; Jiang, J.; Zhang, X.; Cao, D.; Zeng, X. C. Simulation Evidence of Nanobubble Clusters of Gas in Water: A Nanoscale Solvation Mechanism. *J. Am. Chem. Soc.* **2025**, *147*, 28748−28757.
(46) Gao, Y.; Zhang, P.; Luo, H.; Chen, C.; Niu, J.; Tang, Y.; Wang, R.; Li, M.; Xu, X.; Sun, C. Thermal Response of Nanobubble Suspensions Under Freeze−Thaw Cycles through Experiment and Molecular Dynamics Simulations. *ACS Appl. Mater. Interfaces* **2025**, *17*, 67284−67294.
(47) Li, Y.; Sun, T.; Cai, J.; Wang, B.; Li, M. Aging Dynamics of Bulk Nanobubbles Under Pressure Oscillations. *J. Colloid Interface Sci.* **2026**, *708*, 139757.
(48) Zeng, J.; et al. DeePMD-kit V3: A Multiple-Backend Framework for Machine Learning Potentials. *J. Chem. Theory Comput.* **2025**, *21*, 4375−4385.
(49) Xu, K.; et al. GPUMD 4.0: A High-Performance Molecular Dynamics Package for Versatile Materials Simulations With Machine-Learned Potentials. *Mater. Genome Eng. Adv.* **2025**, *3*, No. e70028.
(50) Batatia, I.; et al. A Foundation Model for Atomistic Materials Chemistry. *J. Chem. Phys.* **2025**, *163*, 184110.
(51) Zhang, P.; Gardini, A. T.; Xu, X.; Parrinello, M. Intramolecular and Water Mediated Tautomerism of Solvated Glycine. *J. Chem. Inf. Model.* **2024**, *64*, 3599−3604.
(52) Zhang, P.; Xu, X. Propensity of Water Self-Ions at Air (Oil)−Water Interfaces Revealed by Deep Potential Molecular Dynamics With Enhanced Sampling. *Langmuir* **2025**, *41*, 3675−3683.
(53) Zhang, P.; Xu, X. Modulation of electric field and interface on competitive reaction mechanisms. *J. Chem. Theory Comput.* **2025**, *21*, 6584−6593.
(54) Zhang, Y.; Wang, H.; Chen, W.; Zeng, J.; Zhang, L.; Wang, H.; E, W. DP-GEN: A Concurrent Learning Platform for the Generation of Reliable Deep Learning Based Potential Energy Models. *Comput. Phys. Commun.* **2020**, *253*, 107206.
(55) Fan, Z.; Zeng, Z.; Zhang, C.; Wang, Y.; Song, K.; Dong, H.; Chen, Y.; Ala-Nissila, T. Neuroevolution Machine Learning Potentials: Combining High Accuracy and Low Cost in Atomistic Simulations and Application to Heat Transport. *Phys. Rev. B* **2021**, *104*, 104309.
(56) Liang, T. et al. NEP89: Universal Neuroevolution Potential for Inorganic and Organic Materials Across 89 Elements. *Nat. Comput. Sci.* **2026**. DOI: 10.1038/s43588-026-01009-6.
(57) Fan, Z.; et al. GPUMD: A Package for Constructing Accurate Machine-Learned Potentials and Performing Highly Efficient Atomistic Simulations. *J. Chem. Phys.* **2022**, *157*, 114801.
(58) Shin, D.; Park, J. B.; Kim, Y.-J.; Kim, S. J.; Kang, J. H.; Lee, B.; Cho, S.-P.; Hong, B. H.; Novoselov, K. S. Growth dynamics and gas transport mechanism of nanobubbles in graphene liquid cells. *Nat. Commun.* **2015**, *6*, 6068.
(59) Plimpton, S. Fast Parallel Algorithms for Short-Range Molecular Dynamics. *J. Comput. Phys.* **1995**, *117*, 1−19.
(60) Kresse, G.; Furthmüller, J. Efficient Iterative Schemes for *Ab Initio* Total-Energy Calculations Using a Plane-Wave Basis Set. *Phys. Rev. B* **1996**, *54*, 11169.
(61) Zheng, L.; Chen, M.; Sun, Z.; Ko, H.-Y.; Santra, B.; Dhuvad, P.; Wu, X. Structural, Electronic, and Dynamical Properties of Liquid Water by *Ab Initio* Molecular Dynamics Based on SCAN Functional Within the Canonical Ensemble. *J. Chem. Phys.* **2018**, *148*, 164505.
(62) Chen, M.; Ko, H.-Y.; Remsing, R. C.; Calegari Andrade, M. F.; Santra, B.; Sun, Z.; Selloni, A.; Car, R.; Klein, M. L.; Perdew, J. P.; Wu, X. *Ab Initio* Theory and Modeling of Water. *Proc. Natl. Acad. Sci. U. S. A.* **2017**, *114*, 10846−10851.
(63) LaCount, M. D.; Gygi, F. Ensemble First-Principles Molecular Dynamics Simulations of Water Using the SCAN Meta-GGA Density Functional. *J. Chem. Phys.* **2019**, *151*, 164101.

(64) Zhang, P.; Feng, M.; Xu, X. Double-Layer Distribution of Hydronium and Hydroxide Ions in the Air−Water Interface. *ACS Phys. Chem. Au* **2024**, *4*, 336−346.
(65) Zhang, P.; Chen, C.; Feng, M.; Sun, C.; Xu, X. Hydroxide and Hydronium Ions Modulate the Dynamic Evolution of Nitrogen Nanobubbles in Water. *J. Am. Chem. Soc.* **2024**, *146*, 19537−19546.
(66) Zhang, P.; Gao, Y.; Chen, C.; Guo, X.; Sun, C.; Xu, X. Nanobubble Nucleation and Dissolution Near the Anatase (101)−Water Interface. *J. Am. Chem. Soc.* **2026**, *148*, 18507−18517.
(67) Eldar, Y.; Lindenbaum, M.; Porat, M.; Zeevi, Y. Y. The Farthest Point Strategy for Progressive Image Sampling. *IEEE Trans. Image Process.* **1997**, *6*, 1305−1315.
(68) Ma, R.; Baradwaj, N.; Nomura, K.-i.; Krishnamoorthy, A.; Kalia, R. K.; Nakano, A.; Vashishta, P. Alkali Hydroxide (LiOH, NaOH, KOH) in Water: Structural and Vibrational Properties, Including Neutron Scattering Results. *J. Chem. Phys.* **2024**, *160*, 134309.
(69) Heuft, J.; Meijer, E. A Density Functional Theory Based Study of the Microscopic Structure and Dynamics of Aqueous HCl Solutions. *Phys. Chem. Chem. Phys.* **2006**, *8*, 3116−3123.
(70) Sharma, K.; Adhikari, N. P. Temperature Dependence of Diffusion Coefficient of Nitrogen Gas in Water: A Molecular Dynamics Study. *Int. J. Mod. Phys. B* **2014**, *28*, 1450084.
(71) Easteal, A. J.; Price, W. E.; Woolf, L. A. Diaphragm cell for high-temperature diffusion measurements. Tracer diffusion coefficients for water to 363 K. *J. Chem. Soc., Faraday Trans. 1* **1989**, *85*, 1091−1097.
(72) Gartner, T. E., III; Zhang, L.; Piaggi, P. M.; Car, R.; Panagiotopoulos, A. Z.; Debenedetti, P. G. Signatures of a Liquid−Liquid Transition in an *Ab Initio* Deep Neural Network Model for Water. *Proc. Natl. Acad. Sci. U. S. A.* **2020**, *117*, 26040−26046.
(73) Sanchez-Burgos, I.; Muniz, M. C.; Espinosa, J. R.; Panagiotopoulos, A. Z. A Deep Potential Model for Liquid−Vapor Equilibrium and Cavitation Rates of Water. *J. Chem. Phys.* **2023**, *158*, 184504.
(74) Calegari Andrade, M.; Car, R.; Selloni, A. Probing the Self-Ionization of Liquid Water With *Ab Initio* Deep Potential Molecular Dynamics. *Proc. Natl. Acad. Sci. U. S. A.* **2023**, *120*, No. e2302468120.
(75) Bernetti, M.; Bussi, G. Pressure Control Using Stochastic Cell Rescaling. *J. Chem. Phys.* **2020**, *153*, 114107.
(76) Bussi, G.; Donadio, D.; Parrinello, M. Canonical Sampling through Velocity Rescaling. *J. Chem. Phys.* **2007**, *126*, 014101.
(77) Lee, T.; Judge, G.; Takayama, T. On Estimating the Transition Probabilities of a Markov Process. *Am. J. Agric. Econ.* **1965**, *47*, 742−762.
(78) Knipping, E.; Lakin, M.; Foster, K.; Jungwirth, P.; Tobias, D.; Gerber, R.; Dabdub, D.; Finlayson-Pitts, B. Experiments and Simulations of Ion-Enhanced Interfacial Chemistry on Aqueous NaCl Aerosols. *Science* **2000**, *288*, 301−306.
(79) Wang, G.; et al. Atmospheric Sulfate Aerosol Formation Enhanced by Interfacial Anions. *PNAS Nexus* **2025**, *4*, pgaf058.
(80) Litman, Y.; Chiang, K.-Y.; Seki, T.; Nagata, Y.; Bonn, M. Surface Stratification Determines the Interfacial Water Structure of Simple Electrolyte Solutions. *Nat. Chem.* **2024**, *16*, 644−650.
(81) Li, J.; Wang, F. Surface Penetration Without Enrichment: Simulations Show Ion Surface Propensities Consistent With Both Elevated Surface Tension and Surface Sensitive Spectroscopy. *J. Phys. Chem. B* **2019**, *123*, 7197−7203.
(82) Tian, C.; Byrnes, S. J.; Han, H.-L.; Shen, Y. R. Surface Propensities of Atmospherically Relevant Ions in Salt Solutions Revealed by Phase-Sensitive Sum Frequency Vibrational Spectroscopy. *J. Phys. Chem. Lett.* **2011**, *2*, 1946−1949.
(83) Yang, J.; Zhao, G.; Yin, H.; Feng, Y.; Zhang, P. Effects of CSH Gel Surface Structure on Sodium Chloride Evaporation Crystallization in CSH Gel Nanopores With Molecular Dynamics Analysis. *Appl. Surf. Sci.* **2023**, *639*, 158159.
(84) Anousheh, N.; Shamloo, A.; Jalili, S.; Tuszynski, J. A. Electrolyte Adsorption in Graphene and Hexagonal Boron Nitride Nanochannels. *J. Mol. Liq.* **2022**, *367*, 120474.
(85) Döpke, M. F.; Lützenkirchen, J.; Moultos, O. A.; Siboulet, B.; Dufrêche, J.-F.; Padding, J. T.; Hartkamp, R. Preferential Adsorption in Mixed Electrolytes Confined by Charged Amorphous Silica. *J. Phys. Chem. C* **2019**, *123*, 16711−16720.
(86) Ma, X.; Li, M.; Pfeiffer, P.; Eisener, J.; Ohl, C.-D.; Sun, C. Ion Adsorption Stabilizes Bulk Nanobubbles. *J. Colloid Interface Sci.* **2022**, *606*, 1380−1394.
(87) Jedlovszky, P.; Vincze, Á.; Horvai, G. New Insight into the Orientational Order of Water Molecules at the Water/1, 2-Dichloroethane Interface: A Monte Carlo Simulation Study. *J. Chem. Phys.* **2002**, *117*, 2271−2280.
(88) Kessler, J.; Elgabarty, H.; Spura, T.; Karhan, K.; Partovi-Azar, P.; Hassanali, A. A.; Kuhne, T. D. Structure and Dynamics of the Instantaneous Water/Vapor Interface Revisited by Path-Integral and Ab Initio Molecular Dynamics Simulations. *J. Phys. Chem. B* **2015**, *119*, 10079−10086.
(89) Pezzotti, S.; Serva, A.; Gaigeot, M.-P. 2D-HB-Network at the Air-Water Interface: A Structural and Dynamical Characterization by Means of *Ab Initio* and Classical Molecular Dynamics Simulations. *J. Chem. Phys.* **2018**, *148*, 174701.
(90) Luzar, A.; Chandler, D. Hydrogen-Bond Kinetics in Liquid Water. *Nature* **1996**, *379*, 55−57.
(91) Rapaport, D. Hydrogen Bonds in Water. *Mol. Phys.* **1983**, *50*, 1151−1162.

https://doi.org/10.1021/jacs.6c08865
J. Am. Chem. Soc. 2026, 148, 32412−32425